

Quantum chemical simulation of transient absorption spectroscopy in the CP29 light-harvesting complex

Piermarco Saraceno,¹ Vladislav Slama,¹ and Lorenzo Cupellini*¹

Dipartimento di Chimica e Chimica Industriale, University of Pisa, via G. Moruzzi 13, 56124, Pisa, Italy

(*Electronic mail: lorenzo.cupellini@unipi.it)

Transient absorption spectroscopy is among the most valuable methods for investigating the dynamics of excitons in light-harvesting complexes (LHCs). Even in the simplest LHCs, a physical model is needed to interpret transient spectra, as the number of excitation energy transfer (EET) processes occurring at the same time is too large to be disentangled from measurements alone. Physical EET models are commonly built by fittings of the microscopic exciton Hamiltonians and exciton-vibrational parameters, an approach that can lead to biases. Here we present a first-principles strategy to simulate EET and transient absorption spectra in LHCs, combining molecular dynamics and accurate multiscale quantum chemical calculations to obtain an independent estimate of the excitonic structure of the complex. The microscopic parameters thus obtained are then used in EET simulations to obtain the population dynamics and the related spectroscopic signature. We apply this approach to the CP29 minor antenna complex of plants, for which we follow the EET dynamics and transient spectra after excitation in the chlorophyll b region. Our calculations reproduce all the main features observed in the transient absorption spectra and provide independent insight on the excited-state dynamics of CP29. The approach presented here lays the groundwork for the unbiased interpretation of transient spectra in multichromophoric systems.

I. INTRODUCTION

Light-harvesting complexes (LHCs) owe their spectroscopic and photophysical properties to the aggregate of pigments they contain, and to the protein matrix hosting these pigments.¹ The photophysics of LHCs is characterized by excitation energy transfer (EET) processes among the photosynthetic pigments, which allow the absorbed sunlight energy to reach reaction centers.¹⁻⁴ EET is made possible by the excitonic interactions between the pigments and by their interaction with the protein environment.

Several spectroscopic techniques can be used to study the photophysics of LHCs.⁵⁻⁷ Among them, transient absorption (TA) spectroscopy is possibly the most common method employed to follow EET processes. The time-resolved spectral features measured in TA are in fact direct fingerprints of the exciton dynamics and EET in LHCs. However, the number and density of excited states in LHCs is such that not all overlapping transient signals can be effectively separated, which prevents a complete interpretation of TA spectra without building an underlying EET model.⁸ A possible strategy to solve this issue is represented by structure-based simulations, where a theoretical model is used to simulate EET in LHCs and the corresponding spectral features. In these simulations, the Hamiltonian of the LHC is commonly derived by combining structural and spectroscopic information to fit microscopic parameters.⁹⁻¹⁶ This strategy has proven successful in determining model Hamiltonians for a number of LHCs, but it suffers from some limitations. Firstly, the theoretical framework connecting the microscopic Hamiltonian to the spectroscopic response is necessarily approximated,^{17,18} which could result in biased estimation of the microscopic parameters. Secondly, the spectroscopic information may not be enough to uniquely determine the microscopic parameters, leaving some room for uncertainty.

Atomistic descriptions that directly calculate the exciton

Hamiltonian represent an alternative approach that does not rely on experimental spectroscopic data.¹⁸⁻²⁴ One such strategy is based on a combination of classical molecular dynamics (MD) to sample the structural ensemble of the LHCs in their environment and multiscale quantum mechanics/molecular mechanics (QM/MM) calculations of the Hamiltonian in this ensemble.^{24,25} The microscopic parameters calculated in this way have proven successful in reproducing the linear optical spectra of several LHCs.²⁶⁻²⁹

Here we set to extend this *ab initio* strategy to the simulation of EET dynamics in LHCs and of the corresponding TA spectroscopy. We employ polarizable QM/MM (QM/MMPol)³⁰ calculations of the exciton system to build a reliable model of the LHC, which is then used in conjunction with the Redfield-Förster approach to simulate the population dynamics upon excitation. Finally, a lineshape theory is used to compute the TA fingerprint of population evolution, providing a connection with spectroscopy. A similar strategy was used to simulate two-dimensional electronic spectroscopy maps focusing on short delay times.³¹ Here instead we focus on simulating the time evolution of TA spectra in the picosecond time scale, as such evolution reflects the underlying EET dynamics.

We apply our strategy to CP29, one of the minor LHCs in the photosystem II of plants.⁴ Like other LHCs, CP29 consists in a protein with three transmembrane helices, two minor amphipathic helices and two loops (Figure 1). The protein scaffold embeds 13 chlorophylls (Chls), of which 9 chlorophylls of type a (Chl a), 4 chlorophylls of type b (Chl b), and three carotenoids.³²⁻³⁵ A further Chl a (a616) was found between CP29 and the PSII core in the Cryo-EM structure of the PSII supercomplex.³⁴ Two terminal-emitter domains, Chls a610-a611-a612 and a602-a603-a609 have been identified in CP29.³⁶⁻³⁸ These are clusters of tightly packed Chls that contribute to the low-energy range of the spectrum. However, how the excited-state population equilibrates, and on

which domain, still has to be determined.

We take advantage of a recent molecular dynamics (MD) simulation of CP29 performed in previous work.³⁹ We first analyze the exciton structure and linear absorption spectra of CP29, assessing the Markov and secular approximations in the lineshape theory. Then we study the equilibrium and dynamics obtained with two flavours of the Redfield-Förster approach. Finally, we simulate the EET dynamics and compare with recent experiments of CP29 in nanodiscs.⁴⁰ Our approach provides a good reproduction of all the TA features observed in the experiment, and allows interpreting the TA dynamics from a microscopic standpoint.

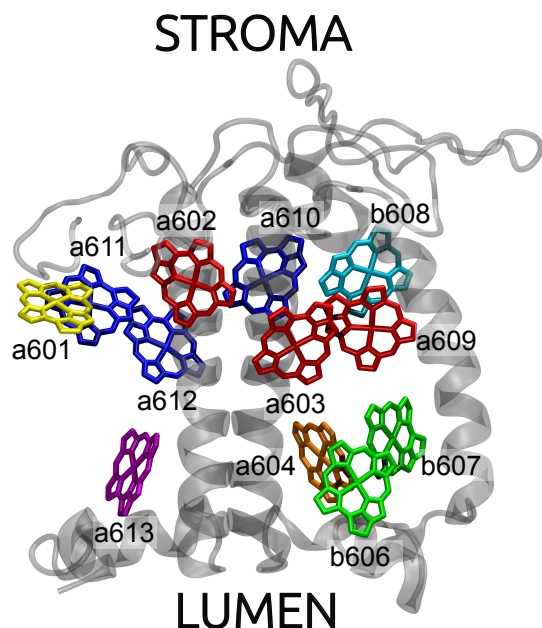


Figure 1. Representation of the Chls embedded in the protein scaffold of CP29. The represented structure is based on the cryo-EM structure of PSI³⁴ and subsequent molecular dynamics.³⁹ The names of the Chlorophyll names and the orientation of CP29 with respect to stroma and lumen are schematically illustrated.

II. THEORY

A. Hamiltonian

The model Hamiltonian for studying the photophysics of multichromophoric aggregates has the form¹⁸

$$\mathcal{H} = \mathcal{H}_{exc} + \mathcal{H}_{vib} + \mathcal{H}_{exc-vib} \quad (1)$$

where \mathcal{H}_{exc} is the purely electronic (excitonic) Hamiltonian, \mathcal{H}_{vib} is the vibrational Hamiltonian, and $\mathcal{H}_{exc-vib}$ represents the system-bath coupling between electronic and vibrational degrees of freedom.

The electronic part is described within the framework of the Frenkel exciton model. Assuming one excited state per

chromophore, the exciton Hamiltonian reads:

$$\hat{\mathcal{H}}_{exc} = \sum_i \varepsilon_i |i\rangle \langle i| + \sum_{i \neq j} V_{ij} |i\rangle \langle j| \quad (2)$$

where $|i\rangle$ is the wavefunction of an excited state localized on the i -th chromophore, whose excitation energy is ε_i , called site energy. V_{ij} is the excitonic coupling between the i -th and the j -th pigment. The eigenstates $|a\rangle$ of the exciton Hamiltonian have energies E_a and are expressed, in this site basis, as

$$|a\rangle = \sum_i c_{ia} |i\rangle \quad (3)$$

For the sake of clarity, from now on we will use indices a, b, \dots to refer to exciton states, and i, j, \dots to refer to site-localized states.

Assuming harmonic vibrational degrees of freedom linearly coupled to the excitations, all information on the exciton-vibrational coupling of pigment i is contained in the spectral density $J_i(\omega)$ or, equivalently, in the energy gap correlation function $C_i(t)$, which quantifies the nuclear-dependent fluctuation of the site energies

$$C_i(t) = \frac{1}{\pi} \int_0^\infty d\omega \left[\coth\left(\frac{\beta\omega}{2}\right) \cos(\omega t) - i \sin(\omega t) \right] J_i(\omega) \quad (4)$$

(we have set $\hbar = 1$). We furthermore assume that the fluctuations of site energies are uncorrelated, and we neglect the fluctuations of exciton couplings.

The total strength of the exciton-vibrational coupling can be quantified by the reorganization energy λ_i :

$$\lambda_i = \int_0^\infty d\omega \frac{J_i(\omega)}{\pi\omega} \quad (5)$$

In practice, the spectral density only accounts for dynamic disorder, that is, nuclear motion inducing fast fluctuations of the site energies. To introduce static disorder, we consider an inhomogeneous ensemble of site energies ε_i and couplings V_{ij} , which is sampled from MD simulations (see Section S2).²⁵

As the matrix elements of the exciton Hamiltonian experience random shifts in the disordered ensemble, the exciton states depend on the specific realization of the disorder. To analyze the exciton structure in the disordered ensemble, we propose the following ‘‘participation ratio’’ matrix, calculated in the site basis:

$$\text{PR}_{ij} = \sum_a^{\text{excitons}} |c_{ia}|^2 |c_{ja}|^2 \quad (6)$$

this quantity measures (for $i \neq j$) how much two sites i and j participate to the same excitons, whereas for $i = j$ it measures how localized are the excitons in which site i participates. PR_{ij} can be easily averaged over the static disorder, as $\langle \text{PR}_{ij} \rangle_{\text{dis}}$, since the site basis does not depend on the realization of the disorder. Thus, $\langle \text{PR}_{ij} \rangle_{\text{dis}}$ provides a measure of delocalization among chromophores. Under the same line of reasoning, we employ the vertical exciton state pigment distribution function^{36,38,41}:

$$d_i(\omega) = \left\langle \sum_a |c_{ia}|^2 \delta(\omega - \omega_a) \right\rangle_{\text{dis}} \quad (7)$$

where $E_a = \hbar\omega_a$ is the energy of exciton a . The function $d_i(\omega)$ measures how much pigment i contributes to excitons with energy $\hbar\omega$. In practice, for visualization we substitute $\delta(\omega - \omega_a)$ with a finite-width Gaussian function.

B. Linear spectra

1. Full cumulant expansion

To compute linear and nonlinear spectra we use the second-order cumulant expansion formalism. For linear spectra, the most general expression is the full cumulant expansion (FCE).^{42,43} In FCE, the linear absorption of the excitonic system is given by

$$A(\omega) \propto \omega \Re \int_{-\infty}^{+\infty} dt e^{-i\omega t} \sum_{ij} \mathbf{I}_{ij}(t) \mathbf{M}_{ij} \quad (8)$$

where $\mathbf{M}_{ij} = \vec{\mu}_i \cdot \vec{\mu}_j$ is the dipole strength matrix. This expression is valid in any basis (site or exciton), as both \mathbf{M} and $\mathbf{I}(t)$ can be transformed from the site to the exciton basis as, e.g., $\mathbf{I}^{\text{site}} = \mathbf{c}^{\text{exc}} \mathbf{c}^\dagger$,⁴⁴ where \mathbf{c} is the matrix of exciton coefficients. The absorption tensor $\mathbf{I}(t)$ can be calculated as:

$$\mathbf{I}(t) = e^{-iH_{\text{el}}t} e^{-\mathbf{K}(t)} \quad (9)$$

where $\mathbf{K}(t)$ is the lineshape matrix, defined in the exciton basis:

$$K_{ab} = \sum_c \sum_i c_{ia}^* |c_{ic}|^2 c_{ib} \int_0^t dt_2 \int_0^{t_2} dt_1 e^{i\omega_{ac}t_2 - i\omega_{bc}t_1} C_i(t_1) \quad (10)$$

Here, $\hbar\omega_{ac} = E_a - E_c$ is the exciton energy difference and $C_i(t)$ is the autocorrelation function of the energy gap for chromophore i (eq. 4). Notably, the FCE lineshape accounts for all off-diagonal ($a \neq b$) terms in the cumulant expansion, also denoted nonsecular terms.⁴⁴

To analyze the contribution of each chromophore to the spectrum, we first define the contribution $A_{ij}(\omega)$ of the i, j pair in the site basis:

$$A_{ij}(\omega) \propto \omega \Re \int_{-\infty}^{+\infty} dt e^{-i\omega t} \mathbf{I}_{ij}(t) \mathbf{M}_{ij} \quad (11)$$

Then, we take $A_i(\omega) = \sum_j A_{ij}(\omega)$ as the contribution of chromophore i . Since $A_{ij}(\omega)$ is a symmetric matrix, this sum exactly contains the diagonal $i = j$ contribution of each chromophore plus half the off-diagonal contribution of the i, j pair.

2. Markov and secular approximations

Making the secular approximation, i.e. dropping all terms $a \neq b$, and remaining in the exciton basis, one arrives at the following expression for the lineshape^{44,45}

$$A(\omega) = \omega \sum_a \mu_a^2 \Re \int_{-\infty}^{+\infty} dt e^{-i(\omega_a - \omega)t} e^{-g_a(t)} e^{-\xi_a(t)} \quad (12)$$

where the term $g_a(t)$ arises from the diagonal (in the exciton basis) terms of the exciton-vibrational coupling, whereas $\xi_a(t)$ arises from the off-diagonal ones. The diagonal term is simply the lineshape function of exciton a ,

$$g_a(t) = \sum_i |c_{ia}|^4 \int_0^t dt_2 \int_0^{t_2} dt_1 C_i(t_1) \quad (13)$$

whereas the off-diagonal term is⁴⁴⁻⁴⁶

$$\xi_a(t) = \sum_{b \neq a} \sum_i |c_{ia}|^2 |c_{ib}|^2 \int_0^t dt_2 \int_0^{t_2} dt_1 e^{i\omega_{ab}t_1} C_i(t_1) \quad (14)$$

This expression for the lineshape was first developed by Renger and Marcus⁴⁶ using the partial ordering prescription of the cumulant expansion, and then renamed as complex time-dependent Redfield theory.⁴⁵

It is customary at this point to apply the Markov approximation only to the off-diagonal fluctuation term⁴⁶, obtaining

$$\xi_a(t) \simeq t \sum_{b \neq a} \sum_i |c_{ia}|^2 |c_{ib}|^2 \int_0^\infty dt_1 e^{i\omega_{ab}t_1} C_i(t_1) = \gamma_a t \quad (15)$$

Thus, the Markovian expression for the contribution of exciton a to the absorption spectrum is⁴⁶

$$A_a(\omega) \propto \omega \mu_a^2 \Re \int_{-\infty}^{+\infty} dt e^{-i(\omega_a - \omega)t - g_a(t) - \gamma_a t} \quad (16)$$

so that $A(\omega) = \sum_a A_a(\omega)$. One can see that $\gamma_a = \frac{1}{2} \sum_{b \neq a} R_{ba}$, where

$$R_{ba} = \sum_i |c_{ia}|^2 |c_{ib}|^2 \left(J_i(\omega_{ba}) + \frac{1}{\pi} \mathcal{P} \int_{-\infty}^{\infty} d\omega \frac{J(\omega)}{\omega_{ba} - \omega} \right) \quad (17)$$

where \mathcal{P} denotes the principal value. The real part of R_{ba} corresponds to the Redfield $a \rightarrow b$ transfer rate.⁴⁵ Crucially, the off-diagonal dephasing rate γ_a is always a complex quantity, which obeys the symmetries of quantum correlation functions. Accounting for the off-diagonal fluctuations by the Redfield rate thus corresponds to neglecting the imaginary part of γ_a . However, this imaginary part results in a reorganization energy shift of exciton energies, in general by different amounts. These shifts were proven to be significant both in model systems⁴⁵ and for realistic spectral densities,⁴³ and they are important for obtaining accurate peak positions. Accordingly, we employ the Markovian expression (16) including the imaginary shift for simulating the spectra. We denote this expression ‘‘complex Redfield’’ (cR) in analogy to Ref. 45. In addition, in this work we will also employ its imaginary version, denoted with ‘‘imaginary Redfield’’ (iR), where the real part of the dephasing γ_a is neglected. The iR approximation accounts for the effect of off-diagonal fluctuations on the peak positions, but neglects the corresponding broadening.

Also in the secular case, we can reconstruct the contribution of the i, j pair to the absorption spectrum as:

$$A_{ij}(\omega) = M_{ij} \sum_a c_{ia} c_{ja} \Re \int_{-\infty}^{+\infty} dt e^{-i(\omega_a - \omega)t - g_a(t) - \gamma_a t} \quad (18)$$

and sum over the columns of A_{ij} to obtain the contribution of each chromophore as detailed above.

C. Transient absorption spectra

To efficiently compute TA spectra for delay times up to tens of ps, we employ the doorway-window and secular approximations.⁴⁷ Furthermore, we neglect the coherent term of the response, and compute only the sequential term, which is related to population evolution during the waiting time t_2 .⁴⁷ This approximation has been commonly used for TA simulations of multichromophoric systems,^{9,11,13,46,48} and corresponds to assuming that vibrational relaxation is much faster than the delay time t_2 between the pump and the probe.⁴⁶

The third-order transient absorption signal at a probe frequency ω can be expressed as a sum of ground-state bleaching (GSB), stimulated emission (SE), and excited-state absorption (ESA):

$$\text{GSB}(\omega) = \sum_a A_a^{\text{GSB}}(\omega) \sum_b \mathcal{D}_{bb}^S(0) \quad (19a)$$

$$\text{SE}(\omega, t_2) = \sum_a A_a^{\text{SE}}(\omega) \mathcal{D}_{aa}^S(t_2) \quad (19b)$$

$$\text{ESA}(\omega, t_2) = \sum_a A_a^{\text{ESA}}(\omega) \mathcal{D}_{aa}^S(t_2) \quad (19c)$$

where \mathcal{D}_{bb} is the doorway amplitude of exciton b created by the pump pulse, therefore \mathcal{D} represents a scaled version of the density matrix created by the pump pulse. The time evolution of the doorway amplitude during the waiting time t_2 is simply given by the density matrix propagator, here computed in the combined Redfield-Förster approach (see Section IID) in the exciton basis. Here we neglect the relaxation to the ground state, therefore the GSB term is time-independent.

The window response functions for each exciton can be written directly in the frequency domain, where we ignore the pulse shape for the probe pulse. The doorway population of exciton a created by the pump pulse is determined by the overlap between the pump and the absorption spectrum of exciton a .^{48,49}

$$\mathcal{D}_{aa}(0) = \int_0^\infty d\omega A_a(\omega) \varepsilon(\omega) \quad (20)$$

where $\varepsilon(\omega)$ is the pump pulse spectrum. The expression for GSB is identical to the linear absorption spectrum in the Markovian secular case

$$A_a^{\text{GSB}}(\omega) \propto \omega \mu_a^2 \Re \int_{-\infty}^{+\infty} dt e^{-i(\omega_a - \omega)t - g_a(t) - \gamma_a t} \quad (21)$$

The SE term corresponds to an emission lineshape

$$A_a^{\text{SE}}(\omega) \propto \omega \mu_a^2 \Re \int_{-\infty}^{+\infty} dt e^{-i(\omega_a - 2\lambda_a - \omega)t - g_a^*(t) - \gamma_a t} \quad (22)$$

where λ_a is the reorganization energy of exciton a . Finally, the ESA contribution is

$$A_a^{\text{ESA}}(\omega) \propto \omega \sum_q \mu_{aq}^2 \Re \int_{-\infty}^{+\infty} dt e^{-i(\omega_{aq} - \omega)t} \times e^{-g_a(t) - g_q(t) + 2g_{aq}(t) + 2i(\lambda_{aq} - \lambda_a)t - \gamma_{aq}t} \quad (23)$$

where q are the double exciton states, μ_{aq} are the transition dipoles between single-exciton and double-exciton manifolds, and ω_{aq} is the corresponding transition frequency, and the dephasing term is $\gamma_{aq} = \gamma_q + \gamma_a^*$. The expressions for the double exciton energies, μ_{aq} , and ESA lineshape functions are given in Section S1. In analogy to the linear response case, we denote this level of theory as “complex Redfield” if both the real and imaginary parts of γ_a/γ_{aq} are included, and as “imaginary Redfield” if the real part is neglected. We note that complex Redfield was employed before for nonlinear spectroscopy in the bacterial reaction center.⁵⁰

D. Redfield-Förster approach

We describe the evolution of the reduced density matrix ρ^S with the combined Redfield-Förster approach in the Markov-secular approximation.^{17,51} In this approach, the evolution within strongly coupled excitonic domains is described with secular Redfield theory, whereas the transfer between these domains are described with generalized Förster (GF) theory.^{52,53} The system Hamiltonian is partitioned into a zeroth-order Hamiltonian and a perturbative term, $\mathcal{H}_S = \mathcal{H}_0 + V$, where \mathcal{H}_0 only contains couplings within the exciton domains and V only inter-domain couplings. \mathcal{H}_0 is diagonalized as $\mathcal{H}_0|a\rangle = E_a|a\rangle$ where the excitons $|a\rangle$ are delocalized over a single domain. In the eigenbasis of \mathcal{H}_0 , the evolution of exciton populations is given by

$$\frac{d}{dt} \rho_{aa}^S = \sum_b R_{aa,bb} \rho_{bb}^S \quad (24)$$

where R is the Redfield-Förster tensor. If two exciton states a and b belong to the same domain, the elements of $R_{aa,bb}$ are the Redfield rates

$$R_{aa,bb} = \sum_i |c_{ia}|^2 |c_{ib}|^2 J_i(\omega_{ab}) \quad (25)$$

for $a \neq b$. Conversely, for two excitons belonging to different domains, the generalized Förster rates are used

$$R_{aa,bb} = \frac{2}{\hbar^2} \left| \sum_{ij} c_{ia} c_{jb} V'_{ij} \right|^2 \Re \int_0^\infty e^{-i\omega_{ab}t - 2i\lambda_{bt} - g_b(t) - g_a(t)} dt \quad (26)$$

This formulation for Redfield-Förster combined approach will be denoted simply as RF. However, this expression completely neglects the off-diagonal fluctuations in the generalized Förster rate expression. In the more general multichromophoric Förster theory, the off-diagonal fluctuations are included in the Förster rate.^{42,54} Here, in analogy to the absorption lineshapes, we try to capture the effect of these fluctuations within the secular and Markov approximations. In this framework, the generalized Förster rate reads

$$R_{aa,bb} = \frac{2}{\hbar^2} \left| \sum_{ij} c_{ia} c_{jb} V'_{ij} \right|^2 \times \Re \int_0^\infty dt e^{-i\omega_{ab}t - 2i\lambda_{bt} - g_b(t) - g_a(t) - \gamma_a t - \gamma_b^* t} \quad (27)$$

Here, the dephasing terms $\gamma_{a/b}$ are those defined in eqs. (15) and (16), and again they are in general complex quantities. Including these terms allows us to recover most of the off-diagonal reorganization energy $\lambda_{aa,bb}$. Notably, this correction has an effect on the equilibrium steady state of the Redfield-Förster relaxation tensor, as the imaginary part of $\gamma_{a/b}$ effectively shifts the exciton energies. The equilibrium is given by the Boltzmann populations according to the energies $\tilde{E}_a^{0-0} = E_a - \lambda_a + \Im\gamma_a$, where \Im denotes the imaginary part. In practice, the vertical exciton energies E_a are shifted by the amount $\lambda_a - \Im\gamma_a$ which measures the total system-bath coupling strength of exciton a . For this reason, we denote the Redfield-Förster method employing eq. (27) as λ -shift Redfield-Förster.

E. Computational details

Structure

The structure of CP29 employed in this work is based on a recent cryo-EM structure of Photosystem II.³⁴ We used the results of a MD simulation from a previous work³⁹, where two independent MD simulations of model-membrane-embedded CP29 have been performed. To compute the exciton Hamiltonian, a total of 129 frames were extracted from two MD replicas. During the purification of CP29, a616 is lost because of its interface position.^{38,55} In addition, b614 is not present in the cryo-EM structure of CP29.³⁴ The ratio of Chl a to Chl b inferred from absorption spectra is compatible with the loss of one of the four Chls b present in CP29, which lead Müh et al. to suggest that Chl b614 is lost in solution.³⁶ Furthermore, Guardini et al.⁵⁵ reported that the Chl a/Chl b ratio is 3.01 ± 0.15 , which is again compatible with only three Chls b present in CP29. For these reasons, we exclude b614 in addition to a616 from our calculations.

QM/MMPol calculations

For each MD frame, the site energies were computed using QM/MMPol^{30,56} in a locally modified version of Gaussian 16.⁵⁷ The QM part was treated at the TD-DFT M06-2X/6-31G(d) level, while for the MM part the polarizable Amber force field was employed.⁵⁸ For the excited-state calculations, the Chl ring was treated at the QM level, whereas the phytol tail, the other chromophores, and the protein were described at the MMPol level as a set of point charges and dipole polarizabilities. Moreover, we performed the same TD-DFT calculations without the protein (*in vacuo*) in order to disentangle the fast fluctuations of site energies induced by bond length fluctuation occurring during MD simulations.²⁵ We avoid double-counting of bond length contribution to the site energy disorder by averaging over fast geometric contribution to site energies (see Section S2).^{25,28} The exciton couplings have been computed by direct integration of transition densities from QM/MMPol calculations, including the explicit MMPol contribution to the coupling.⁵⁶

Spectral densities

The spectral densities of Chls a and b were modeled as a sum of one overdamped Brownian oscillator⁵⁹ and A underdamped discrete contributions, $J(\omega) = J^{\text{OBO}}(\omega) + J^d(\omega)$. The discrete part is

$$J_i^d(\omega) = \pi \sum_{\alpha} S_{\alpha,i} \omega_{\alpha,i}^2 [\delta(\omega - \omega_{\alpha,i}) - \delta(\omega + \omega_{\alpha,i})] \quad (28)$$

where $\omega_{\alpha,i}$ is the frequency of the α -th normal mode for pigment i and $S_{\alpha,i}$ is the corresponding Huang-Rhys factor. In practice, the delta-functions are replaced with Lorentzian functions having widths of 5 cm^{-1} . The discrete part of the SD arises from the intramolecular vibrations of the pigments (Details in the Supplementary Material).⁶⁰ To compute normal modes of Chls, first we performed QM/MM optimizations where the pigment of interest is treated at B3LYP/6-31G(d) level, and the rest at MM level using the same force field as in the MD simulations; the same method was next used to compute normal modes. The gradients of the excitation energy computed at the CAM-B3LYP level were used to compute the Huang-Rhys factors. The procedure was repeated for chlorophylls a604, a610 and b608 for 8, 8 and 16 MD frames respectively. The average SDs are reported in Figure S1. The resulting average reorganization energies for the vibrational contribution are 635 cm^{-1} , 551 cm^{-1} , and 729 cm^{-1} for a604, a610 and b608 respectively. Small differences can be highlighted between the SDs of the treated pigments, in terms of peak intensity and position. These differences can be explained considering that the pigments experience slightly different surrounding chemical environments.

The overdamped Brownian oscillator accounts for the motion of the environment, and reads

$$J_i^{\text{OBO}}(\omega) = \pi \lambda_{i,\text{env}} \omega \frac{\gamma_{i,\text{env}}}{\omega^2 + \gamma_{i,\text{env}}^2} \quad (29)$$

where $\lambda_{i,\text{env}}$ and $\gamma_{i,\text{env}}$ are the reorganization energy and the damping constant of the environment respectively. The overdamped Brownian parameters for the environmental SD were taken from previous works.^{9,11} The reorganization energy $\lambda_{i,\text{env}}$ is 37 cm^{-1} and the damping factor used is 30 cm^{-1} , corresponding to a correlation time of $\sim 180 \text{ fs}$. We employed the same contribution for all chls.

For the simulations, the spectral density of all other Chls a has been approximated with the SD of Chlorophyll a610, to avoid the expensive normal-mode evaluation of the SD of each pigment along several each MD frames. For the same reason, the SDs of b606 and b607 were taken equal to that computed for b608.

EET simulation details

The excitonic Hamiltonian of each MD frame has been partitioned according to the clusters obtained by applying a hi-

erarchical clustering algorithm to the participation ratio matrix defined in eq. (6) (see Figure S4b). The resulting clusters are: a602-a603-a609, b606-b607, a610-a611-a612 and all other chlorophylls isolated. This means that the transfer within these clusters is treated using Redfield EET theory, while the transfer to other clusters is modeled using Generalized Förster EET theory.

III. RESULTS AND DISCUSSION

In this section, we will first analyze the ensemble of exciton Hamiltonians obtained with the QM/MMPol calculations. After this, we will compare the results of our spectra simulations with the experiments by Sardar et al. on CP29 in nanodiscs.⁴⁰

A. Exciton Hamiltonian

First, we discuss the exciton Hamiltonian obtained with our QM/MMPol strategy (See Table S1 for the average Hamiltonian). As shown in Figure S2, QM/MMPol average site energies range from about 15400 to 16200 cm^{-1} (600-700 nm). Site energies computed *in vacuo* (i.e. without considering the environment) are always greater than QM/MMPol ones, but the shifts due to the environment show some variation. Chls b have greater site energies than Chls a, and this difference is enhanced by the environment. The magnitude of the solvatochromic effect ranges from -500 cm^{-1} to -100 cm^{-1} .

Among Chls b, b606 is the most blue-shifted one, while b608 is lower in energy than b607 (Table S1). These results partially agree with site energies obtained by a fit of linear spectra,³⁸ where b606 is again the blue-most Chl, but b607 is lower in energy than b608. Conversely, the results by Müh et al. show that b607 and b608 have similar site energies³⁶, which better agrees with our results. At the other end of the energy ladder, Chls a602 and a610 are the lowest energy sites. These chlorophylls belong to the putative terminal-emitter domains of CP29, and have been identified as low-energy sites also in previous work.^{15,36,38,61} However, Chls a611 and a603 have also been assigned to low-energy sites on the basis of spectral fitting.^{36,38} In our calculations Chl a611 is the most blue shifted among Chls a. The site energy location of Chl a604 is debated in the literature. While atomistic calculations place it among the lowest energy sites,^{36,61,62} structure-based spectral fits seem to assign a substantially higher site energy to this Chl.³⁸ In our calculations, Chl a604 is in the mid-energy range. The relative difference between the site energies of Chls of the same type are very small and the role of the protein environment is crucial. For this reason, it is difficult to carry out a robust comparison between different methodologies. We note that some of these calculations are based on the X-ray structure³², which features a Chl in a different position than in the Cryo-EM structure.³⁴

As reported in Figure 2a and Table S1, the largest couplings involve pigment pairs with small center-to-center distance (a611-a612, a603-a609, b606-a604 and b608-a610).

The largest couplings (~ 170 and 130 cm^{-1}) are found for the a611-a612 and a603-a609 pairs, while the largest a/b coupling is a604-b606 (111 cm^{-1}). These couplings are slightly larger compared to previous work,^{36,62,63} although they are similar to the QM/MMPol couplings by Jurinovich et al.⁶²

To characterize the exciton structure in the disordered ensemble, we show in Figure 2c the vertical exciton state pigment distribution functions (eq. 7).⁴¹ These distributions show the density of states of the excitons in which each pigment is involved. Most of the distributions have more than one peak because of the exciton couplings, which cause energy splitting. Chls a601 and a603 present a rather narrow and unimodal distributions, which is expected as these Chls couple weakly to other chromophores. In the low-energy range, Chl a602 contributes to the lowest-energy excitons together with Chl a603, whereas the lowest exciton in the a610-a611-a612 pigment cluster seems slightly higher in energy. This exciton has a significant contribution from Chl a612, which has the third-lowest site energy in our calculations (See Figure S2). Among Chls b, we can see that b608 contributes to the low-energy spectral range, while b606 and b607 have similar energy distributions. These results qualitatively agree with some previous results from the literature.³⁶ Specifically, we confirm that b606 participates to excitons at higher energy than b607 or b608. Among chromophores in the luminal layer, a604 participates to excitons at lower energy than a613.

Exciton delocalization can be analyzed exploiting the participation ratio matrix eq. (6) averaged over the disorder. We display the quantities $\langle \text{PR}_{ij} \rangle_{\text{dis}}$ as lines connecting the pigments in Figure 2b (the map is given in Figure S4a). This gives a different picture than the interpigment couplings of Figure 2a, as $\langle \text{PR}_{ij} \rangle_{\text{dis}}$ also accounts for the energy difference between pigments and for disorder effects. For example, despite the significant a609-b608 coupling, there is limited delocalization between these pigments. Among Chls a, a604 and a613 are the most localized chlorophylls, whereas there is some delocalization within the Chls b, especially between b606 and b607. As expected, there is strong delocalization in both terminal-emitter domains a602-a603-a609 and a610-a611-a612.

B. Absorption spectra

The excitonic parameters presented in the previous section were used for the simulation of linear absorption spectra (OD). The simulations were performed with full cumulant expansion (FCE), complex Redfield (cR) theory and its imaginary version (iR). In this way we assess the Markov-secular approximations that will be employed in the calculations of TA spectra.

In Figure 3a we show the absorption spectra simulated with different lineshape theories. Moving from FCE to cR and iR, the Chl a OD band at 630 nm gets narrower and less red-shifted. This is due to the simplified treatment of the off-diagonal reorganization energy in the Markovian theories, and the complete neglect of the broadening induced by off-diagonal fluctuations. This effect is less evident in the Chl b

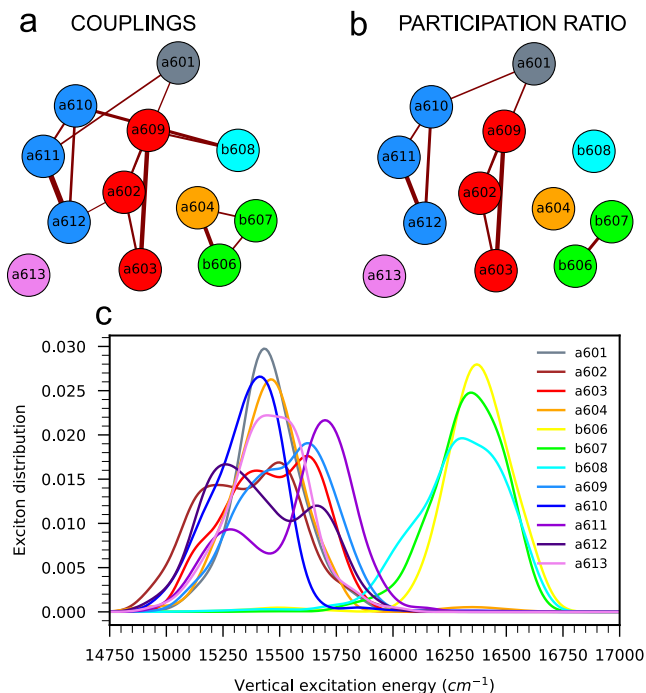


Figure 2. (a) Interpigment coupling network. The stick size represents absolute value of each coupling. Only couplings greater than 17 cm^{-1} are displayed. (b) Participation ratio network. The size of each line is proportional to the relative element of the disorder-averaged participation ratio matrix $\langle \text{PR}_{ij} \rangle_{\text{dis}}$, and measures the delocalization over a pair of pigments. Only participation ratio greater than 0.06 are displayed. (c) Distribution of vertical exciton energies along the MD ensemble. The broadening parameter employed for the Gaussian functions is 150 cm^{-1} (FWHM). In panels (a) and (b), node positions are an in-perspective projection of pigments centers. In panels (b) and (c), the site energies have been shifted by -1069 cm^{-1} for Chl a and -447 cm^{-1} for Chl b to compensate the systematic error of the QM method (see Section III B).

OD band at 580 nm, because of the overlap with the vibrational sideband of Chl a absorption band. Moreover, we note that the intensity of the Chl a OD vibrational sideband at 580 nm is underestimated using cR and iR.

In order to compare with experiments, the site energies of Chl a and Chl b were shifted of -1069 cm^{-1} and -447 cm^{-1} respectively in order to correct the systematic error made by our QM/MMPol model on the excitation energies. This error arises mainly from the QM (TD-DFT) method of choice, but in principle also from the inaccuracies in the force-field treatment of Chl geometries.^{25,29} Notably, this shift includes also any error on the treatment of the reorganization energy, therefore it is different for the more approximate theories. The shift for cR is -1105 cm^{-1} and -530 cm^{-1} respectively. The shift for iR is -1115 cm^{-1} and -540 cm^{-1} respectively.

In Figure 3b we report the simulated absorption spectra and compare them to the experiment. The absorption peaks at 677 nm and 640 nm correspond roughly to the 0-0 Q_y absorption band of chlorophylls type a and b respectively. The small band at 590 nm is the vibrational sideband of Chl b, while that of Chl a is hidden between 600 and 640 nm. The Chl a band is

reasonably reproduced by all theories, although it is too broad with FCE and cR, and it is too narrow with iR, which simply neglects homogeneous off-diagonal broadening (lifetime broadening). cR shows much better agreement with experiments than FCE and iR between 600 nm and 640 nm, which corresponds to the Chl b absorption and Chl a vibrational sideband (Figure 3c). Such an unexpected result does not imply a better performance of cR with respect to FCE, as FCE shows superior performance for a wide range of parameters.⁴⁴ On the contrary, this suggests that there are error compensations at play when using cR theory. Specifically, our calculations might overestimate the spectral density of Chl a in the high-frequency region, or the magnitude of static disorder for Chls b. Finally, below 600 nm in the Chl b vibrational sideband, FCE shows slightly better agreement with the experiments than cR and iR.

C. Exciton dynamics and transient absorption

We simulated the transient absorption spectra using the Markovian theory for the determination of doorway and window amplitudes, whereas the density matrix evolution was calculated in the Redfield-Förster formalism. As the iR approximation provided the best agreement with transient absorption experiments (see below), here we mainly discuss the spectra simulated with this theory. To compare with experiments, in the following we used the same site-energy shift determined above for iR theory.

1. Redfield-Förster equilibrium populations

Before investigating the exciton dynamics upon excitation, in Figure 4 we first investigate the equilibrium site populations obtained with the Redfield-Förster approach including or excluding the off-diagonal λ -shift (Equations 26 and 27). We compare the calculated equilibrium populations with the analytical formula by Gelzinis et al.⁶⁴, which has been shown to reproduce the exact equilibrium in the limit of high temperature and slow bath up to intermediate system-bath coupling strengths. Notably, using λ -shift we can achieve much better agreement with the analytical formula. On the other hand, without including this shift in the generalized Förster rate, we overestimate the population of single sites (a601, a604, a613) and underestimate the population of excitonic clusters, such as a610-a611-a612. This effect can be explained considering that the λ -shift accounts for the off-diagonal fluctuations and their reorganization energy. This term decreases the energy of more delocalized excitons, increasing their equilibrium population.

2. Dynamics upon pump excitation

We simulated the EET dynamics upon excitation by a pump pulse in the Chl b region (Figure 5a). We reproduce the pulse of Ref. 40, which is centered at 630 nm and has a duration of

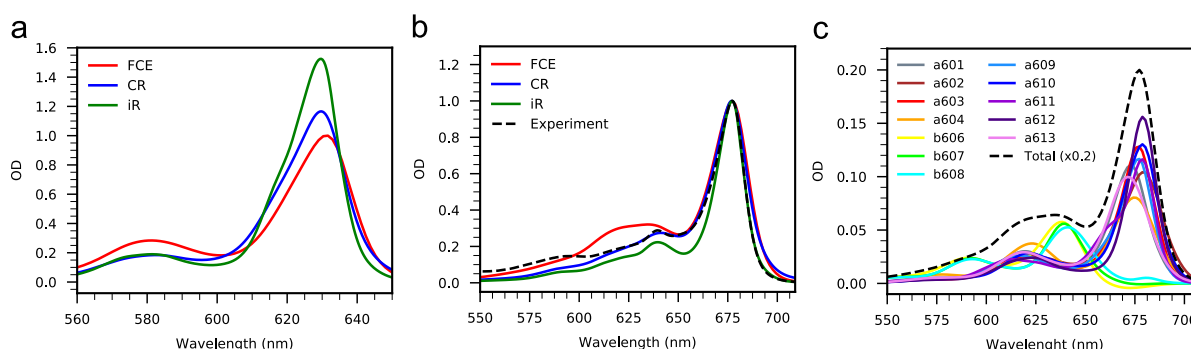


Figure 3. Absorption spectra (OD) of CP29 (283 K). The simulated spectra have been averaged over MD static disorder. (a) Absorption spectra (OD) simulated using different lineshape theories. The spectra have been scaled all by the same factor, so that the FCE maximum is one. (b) Comparison to the experimental spectrum. We have normalized the spectra separately and site energies have been shifted differently for each spectrum so to match the Chl a and Chl b maxima (See text). (c) Contribution of different chromophores to the simulated (FCE) absorption spectrum of CP29 (283 K) (averaged over MD).

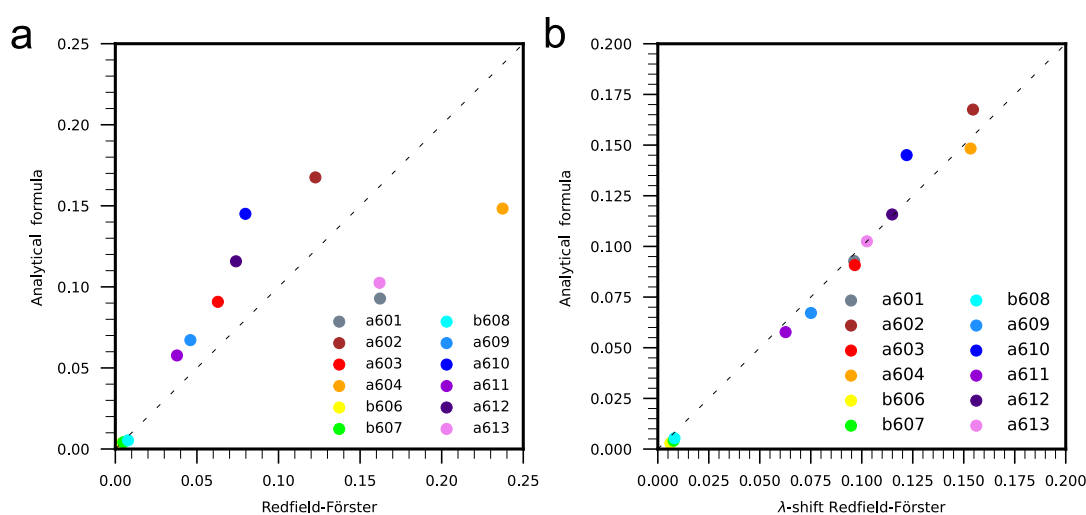


Figure 4. Comparison between the equilibrium site populations obtained with the analytical formula⁶⁴ and those obtained with Redfield-Förster approach (a) without and (b) with λ -shift. The populations are calculated at 283 K and averaged over the MD static disorder.

80 fs (FWHM). Figure 5b shows the population dynamics of the pigment domains. First, the pump excites Chls b606 and b607 and, to a lesser extent, b608. Some Chls a are also excited because of the overlap between the pump and the Chl a vibrational sideband. Mascoli *et al.*³⁸ At short times (<1 ps), the dynamics is dominated by the depopulation of Chls b and the concurrent rise of the population of Chl a604, as well as a610-a611-a612. This subpicosecond time scale matches the transient absorption results.³⁸ On a slower timescale, the domain a602-a603-a609 also populates. Finally, we see a slower decay of the a604 population with a rise of both terminal emitter domains. Chl a604 was first identified as a “bottleneck” site in the EET dynamics of LHCII,^{10,12} and later the same Chl was assigned as a slowly equilibrating site of other LHCs, including CP29.^{13,38} The populations of Chls a601 and a613 only slightly increase during the dynamics, because the initial populations generated by the pump are already close to the equilibrium ones. Finally, the system moves towards equilib-

rium and the two terminal emitter domains acquire most of the population. The a602-a603-a609 pigment cluster becomes the most populated, which is consistent with the fact that Chl a602 contributes the most to the lowest-energy excitons (Figure 2).

The population dynamics of Figure 5b does not allow an immediate interpretation of the energy flow between sites. To better depict how energy is transferred among sites, we define the population flux using the density matrix propagator in the site basis as explained in Appendix A. The resulting net flux $\tilde{\Phi}_{i \rightarrow j}(t \rightarrow t')$ measures the amount of population transferred from site i to site j between times t and t' . The average fluxes are reported in Figure 6 for the time frames 0–1 ps and 1–10 ps. This representation helps interpreting the population dynamics (Figure 5b). The depopulation of Chls b during the first ps occurs mainly through transfer from b606-b607 to Chl a604, while Chl b608 transfers to a610-a611-a612 as well as a602-a603-a609. Then, the population of a604 is transferred mainly to the a602-a603-a609 domain, and in a mi-

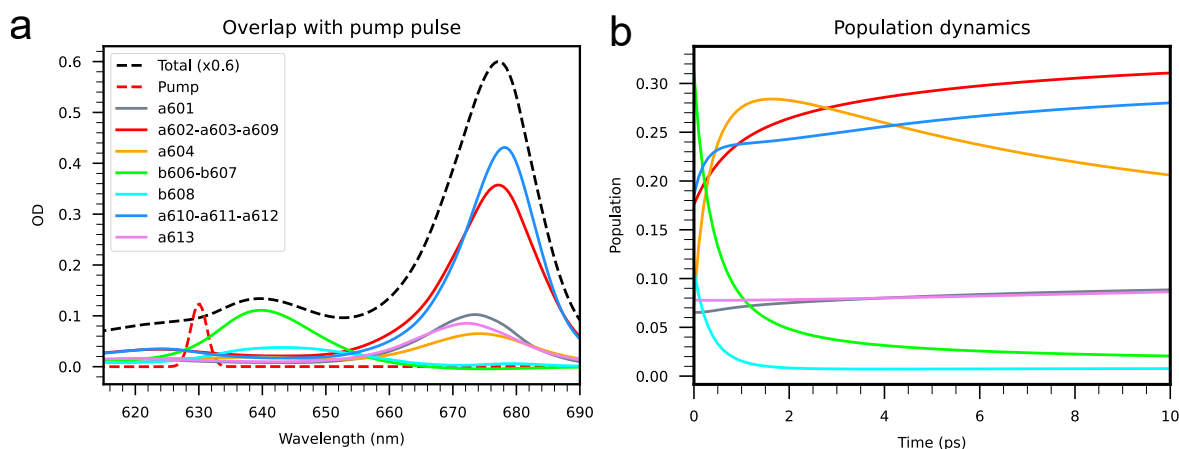


Figure 5. (a) Overlap between the pump pulse (630 nm, 70 fs FWHM) and single-chromophore contribution to spectra obtained with iR (averaged over the MD). (b) Population dynamics of CP29 obtained using Redfield-Förster approach. Different lines correspond to the population of the different pigment domains, represented by the the sum of the corresponding populations. The simulations have been performed at 283 K and averaged over MD static disorder.

nor part to a610-a611-a612. In the 1–10 ps time frame, some equilibration is observed also within both terminal emitter domains.

To determine the characteristic times related to each EET process, we computed effective EET rates between the different domains of CP29. These rates are constructed in order to reproduce the evolution of the site populations with a rate equation, and then lumping the rates together to describe transfers within domains (See Appendix B). The calculated effective rates are reported in Table S2 and can reproduce accurately the population dynamics (see Figure S3). There are three main Chl b \rightarrow Chl a EET pathways: the b606-b607 pair transfers to a604 in \sim 300 fs, whereas b608 transfers to both the a610-a611-a612 cluster in \sim 500 fs and to the a602-a603-a609 cluster in about 2 ps, which is consistent with the results of Figure 5b.

Chl a604 can transfer energy to both terminal emitter domains, a602-a603-a609 and a610-a611-a612. The characteristic EET times from Chl a604 to the other Chls a are slower than 10 ps, although adding all rates results in a depopulation time of a604 faster than 10 ps. Surprisingly, the EET rates between the a602-a603-a609 and a610-a611-a612 domains are quite fast (a few picoseconds), indicating that the population of these domains can easily equilibrate. Finally, a601 is in equilibrium with both terminal emitter domains in the ps time scale, whereas a613 is weakly connected only to a610-a611-a612.

To further investigate the EET network within the Chl a pool, we reported in Figure 7 the excited state dynamics for CP29 if the initial population is set to a604. These results have been obtained using the effective rates shown in Table S2, but they are almost identical to the ones obtained with the full density matrix propagation (Figure S3b). The a602-a603-a609 population increase can be well fitted by a single exponential with a 6 ps time constant. For a610-a611-a612, the time constant is 8 ps. The decay of a604 has to be fitted with a double exponential of time constants 2.5 ps and 12 ps.

These values are lower than the related effective rates, because several simultaneous process occur during the dynamics that involve other chromophores.

3. Transient absorption spectra.

The experimental transient absorption (TA) spectra of CP29 are reported in Figure 8a. The spectra show (i) a strong negative peak (680 nm) arising from Chl a, (ii) a minor negative TA band at 640 nm due to Chl b, and (iii) a minor positive band at 635 nm. Moving to TA dynamics, first, we note that the positive peak at 635 nm quickly (<0.08 ps) disappears, while the intensity of the main Chl a band increases. This spectral feature might be related to vibrational relaxation of Chl a, as supported by the fact that the absorption band of Chl b does not show the same behaviour. Moreover, we note that on a slower timescale (0.08 ps \rightarrow 10 ps) the minor Chl b band (642 nm) disappears while the major Chl a band (682 nm) gets more intense. This spectral feature is related to EET from Chl b to Chl a and might also include relaxation within the Chl a network.

Before discussing more in detail the simulated TA spectra, we analyze the difference between the cR and iR transient absorption lineshapes. TA simulations with cR showed worse agreement with experiments than iR (see Figure S7). The only difference between these two theories is the neglect in iR of the real part of the dephasing γ_a , which is related to the Redfield exciton relaxation rate. This term contributes to broadening all third-order response contributions, but only in the ESA case both the single-exciton and double-exciton relaxation rates contribute to the broadening (see eq. 23). Moving from iR to cR, the ESA contribution broadens more than the GSB, leading to (i) an apparent positive peak at \sim 700 nm and (ii) underestimation of overall intensity evolution of the main TA band when using cR (see Figure S7). We conclude that the Markovian approximation in the ESA contribution over-

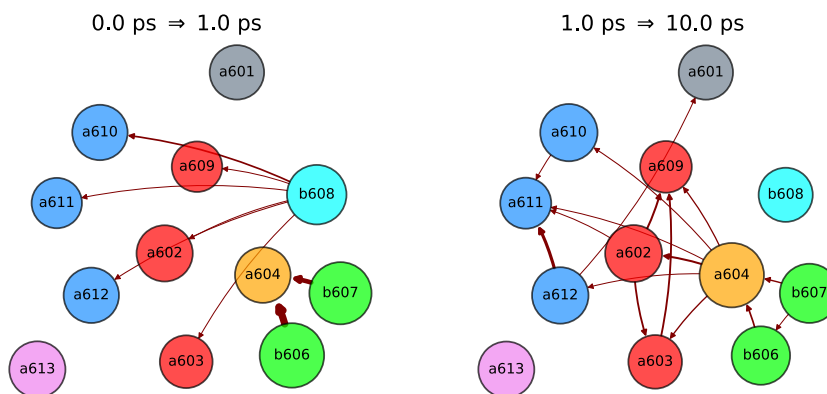


Figure 6. Excitation Energy Transfer flows network in CP29 obtained using the Redfield-Förster approach. The simulations have been performed at 283 K and averaged over MD static disorder. Nodes position represent the in-perspective-position of pigments. Node color has been set according to the same clusters used for the simulations. The width of the arrows is proportional to each net population-to-population flux (only fluxes greater than 0.0011 are displayed in the figure). Node size qualitatively reflects the population of sites at the beginning of each time range.

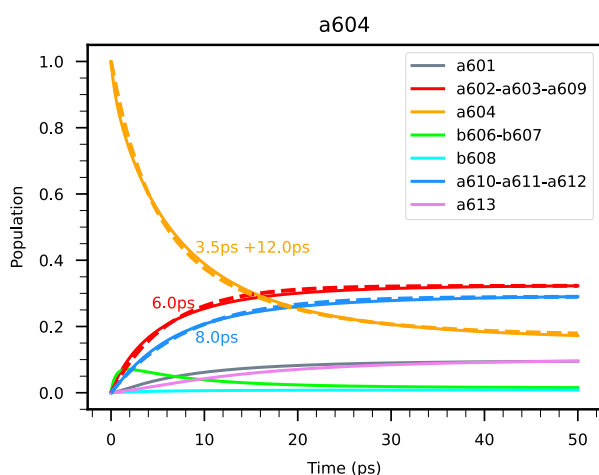


Figure 7. Excited-state dynamics of CP29 obtained with an initial condition where only a604 is excited. The dashed lines are exponential fits whose lifetimes are reported as labels. The simulations have been performed using the effective rates for each realization of the disorder, and then averaged. The population dynamics obtained in this way is almost identical to the reference Redfield-Förster simulations (see Figure S3b).

estimates the broadening due to off-diagonal fluctuations, and it is safer to ignore the real part of the dephasing for simulating nonlinear spectroscopy. A non-Markovian theory should mitigate this problem, but would have greater complexity, especially for the ESA contributions.

The CP29 TA spectra simulated with iR show good agreement with the experiments, in terms of bands lineshape and evolution (Figure 8a,b). For a better comparison, we overlay in Figure 8c the measured and simulated TA spectra at 10 ps delay, roughly corresponding to the excited-state equilibrium.

To exactly compare lineshapes, we matched the main negative Chl a peak in this comparison. The simulated main Chl a band shows an excellent agreement with the experiment, whereas a small discrepancy is found above 690 nm and in the Chl b region. Nonetheless, our simulation essentially reproduces all the spectroscopic features at this delay time.

We now analyze the accuracy of our simulations in reproducing the shift between absorption and TA spectra. Figure 8a shows that in the experiment the TA Chl a and Chl b bands are red-shifted by 6.1 nm and 2.2 nm respectively, while in our simulation the Chl a band is 2.8 nm red-shifted and the Chl b band is 3.7 nm blue-shifted (Figure 8b). These shifts are related to the difference between GSB and ESA, which depends on the exciton energies in the singly and doubly excited manifolds, as well as on the diagonal and off-diagonal fluctuations. Within our formalism, these fluctuations are treated within the secular and Markov approximations. Nonsecular terms appear to reduce the effects of exciton delocalization,⁶⁵ while on the other hand delocalization affects the mismatch between GSB and ESA.⁶⁶ We speculate that the secular approximation employed to calculate the transient absorption lineshape may affect the GSB and ESA peak positions and thus the shift with respect to the ground-state absorption spectrum.

To assess the importance of off-diagonal energy fluctuations, we calculated the transient absorption spectra neglecting all off-diagonal terms altogether, namely, ignoring the dephasing term γ . We will denote this approach as Redfield (diagonal approximation). In these calculations the shift between absorption and TA is not observed at all (Figure S6), which suggests that this shift is related to the off-diagonal reorganization energy. As this part is the most approximate within our iR theory, this is another indication of the possible importance of nonsecular and non-Markov contributions. A more complicated issue is the neglect, in the Redfield-Förster formalism as well as in the lineshape theory, of dynamic localization ef-

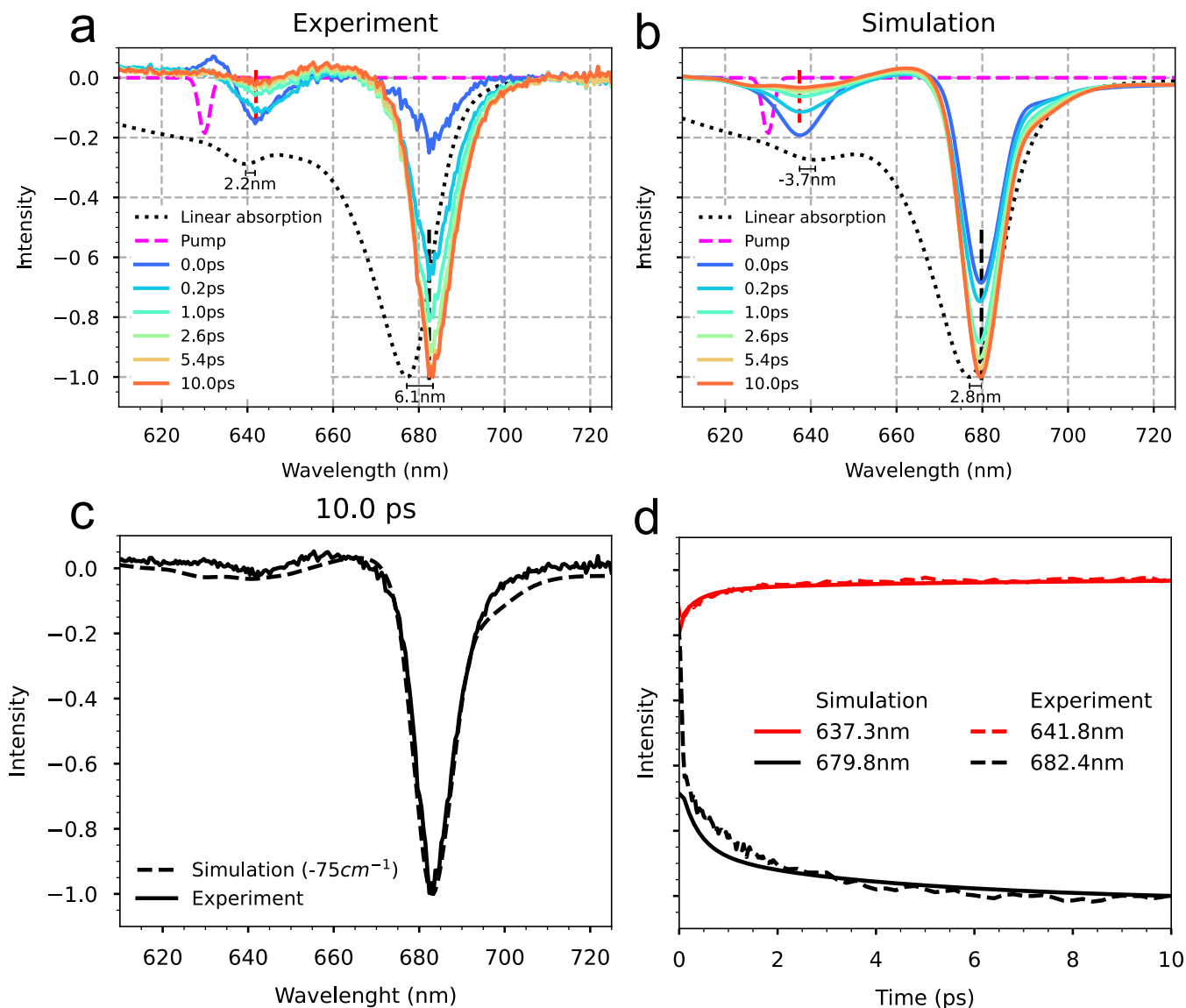


Figure 8. TA spectra of CP29. The simulations have been performed at 283 K of CP29 and averaged over MD. Comparison between (a) experimental and (b) simulated (with the iR approximation) TA spectra. The main Chl a negative peak obtained with the greatest delay time has been normalized to -1 , while the spectra obtained with shorter delay times have been normalized according to their relative intensity. The inverted absorption spectrum is shown as dashed lines, and the shift between the absorption and TA peaks are labeled for both Chl a and Chl b bands. (c) Simulated and experimental TA spectra at fixed delay time (10 ps). The simulated spectra have been shifted in order to better compare the lineshape with the experiment. (d) Simulated and experimental TA spectra at fixed wavelength corresponding to Chl a and Chl b peaks.

fects. Dynamic localization effectively changes the excitons of the system throughout the dynamics,⁶⁷ which possibly results in different GSB/ESA lineshapes.

Figure 8d shows the time evolution of the spectra at selected wavelengths, corresponding to the maxima of Chl b (682.4 nm) and Chl a (641.8 nm) bands. From 0.08 ps to 10 ps there are two different transfer processes, a faster one (0.08 ps to 1 ps) and a slower one (1 ps to 10 ps). Our simulations can reproduce accurately the intensity and evolution of the TA bands. We can highlight some minor discrepancies between simulations and experiments. First, at $t = 0$, the sim-

ulated main Chl a band is more negative than in the experiments. We could expect this, because the Chls a populated by the pump are initially vibrationally excited, and the main Chl a band rises due to vibrational relaxation. In the sequential approximation adopted here, the vibrational relaxation is instantaneous, therefore the main Chl a band is already intense at time zero. Secondly, the first decay process is slightly faster (0.4 ps) than experiments (0.6 ps), while the second one (3.0 ps) seems slower than experiments (2.5 ps).

From the above analysis, the first decay is attributed to the transfer of energy from Chls b to Chls a. The second one

arises from the EET within the Chl a pool, which only slightly affects the intensity of the main Chl a band. As the simulations can reproduce correctly the kinetics of the Chl b band, we could state that the EET transfer process from Chl b to Chl a has been modeled correctly. On the other hand, the kinetics of the Chl a band is reproduced semiquantitatively, as explained above. For this reason, we deduce that the transfer processes that the simulation cannot reproduce quantitatively include some relaxation in the Chl a pool, for example exciton relaxation within a strongly coupled domain. Redfield rates within an exciton domain are generally overestimated,¹² therefore it is not surprising that the dynamics within the first picosecond is too fast in the simulations. It is more difficult to assess the second process, which arises from multiple transfers between a604 and the two terminal emitter domains a602-a603-a609 and a610-a611-a612. These transfers are described with the Generalized Förster rates between domains, and some delocalization effects that enhance EET rates could be missing in this description. Alternatively, the discrepancy in the kinetics could also arise from inaccuracies in the underlying Hamiltonian.

IV. CONCLUDING REMARKS

In this work, we have presented a strategy for the first-principles simulation of excited-state dynamics and transient absorption spectra of light-harvesting complexes. As a test case we considered CP29, one of the minor LHCs in the Photosystem II (PSII) of plants, for which recent measurements of transient absorption are available both in detergent and in nanodiscs.^{38,40} Our strategy builds on accurate atomistic calculations of the exciton Hamiltonian that account for the effect of the protein environment on site energies and couplings. The connection to spectroscopic observables is made with a Markovian lineshape theory,⁴⁶ while exciton dynamics is simulated in the combined Redfield-Förster approach.⁵¹

We have argued that the reorganization effects due to off-diagonal exciton-vibrational interactions should be taken into account, even when employing the secular and Markovian approximations. As these off-diagonal reorganization energies essentially renormalize the energies of exciton states in the same way as the diagonal reorganization energies do, these effects are also important for the calculation of generalized Förster rates. Including off-diagonal fluctuations in the generalized Förster rates leads to an equilibrium state that is closer to the analytically derived equilibrium.⁶⁴ Assessing the equilibrium state with a numerically exact method may be needed to confirm this result more systematically.⁶⁸

The transient absorption spectra calculated in this work agree well with experiments, both in the general shape and in their evolution. Furthermore, direct comparison of time traces at selected wavelengths demonstrates a correct estimation of the main EET time scales. This remarkable result suggests that the approximate methods employed have reasonable accuracy also with realistic exciton couplings and spectral densities. There remain minor deviations with respect to the experiment, especially concerning the position of nega-

tive bands in the TA spectra. We have speculated that this inconsistency arises from the secular approximation used in the calculation of nonlinear spectra. Another source of inaccuracy stems from the Markov approximation, which leads to unphysical broadening of ESA lineshapes. To mitigate this problem, we have decided to ignore the lifetime broadening in transient absorption lineshapes, using only the imaginary part of the off-diagonal contribution.

The good agreement with experiments for time traces suggests that the Redfield-Förster method faithfully reproduces the EET processes in the Chl network of CP29. We have analyzed the EET dynamics by looking at the population flux between different pigments. This has allowed to disentangle the processes occurring at each timescale. The first one consists in fast (<1 ps) EET from b606-b607 to a604 and from b608 to a610-a611-a612. After this, several slower processes (>1 ps) take place, including EET from a604 to all other Chls a and equilibration within the two terminal emitter domains a602-a603-a609 and a610-a611-a612. The thermal equilibrium is established after ~10 ps, consistently with spectroscopic estimations.³⁸

In summary, coupling accurate quantum chemical calculations with simulations of exciton dynamics and nonlinear lineshapes proved to be a viable strategy to complement transient absorption measurements. Our first-principles approach offers an unbiased interpretation of transient absorption measurements in light-harvesting complexes, and holds the promise of disentangling simultaneous photophysical processes occurring in LHCs. Simulations of transient absorption spectra represent a means of quantitatively assessing the exciton Hamiltonians computed with quantum chemical methods. To minimize other sources of inaccuracy, further improvements are still needed. Firstly, it will be fundamental to assess the importance of nonsecular and non-Markovian contributions to the third-order lineshapes. Moreover, a comparison of perturbative dynamics with numerically exact theories⁶⁹⁻⁷¹ or more accurate approximations^{60,72} would be useful to more systematically determine their applicability to both population dynamics and spectral lineshapes.⁷³

SUPPLEMENTARY MATERIAL

See the supplementary material for details on the double exciton manifold and ESA, on the static disorder treatment, and on the normal-mode analysis calculations. Additional figures include the site energy ladder, the participation ratio matrix, a comparison of other approximate TA lineshapes.

ACKNOWLEDGMENTS

We thank Dr. Samim Sardar and Prof. Giulio Cerullo for providing us with the TA measurements of CP29 in nanodiscs. LC and VS acknowledge funding by the European Research Council, under the grant ERC-AdG-786714 (LIFETimeS).

DATA AVAILABILITY STATEMENT

The data that support the findings of this study are available from the corresponding author upon reasonable request.

AUTHOR DECLARATIONS

Conflict of interest

The authors have no conflicts to disclose

Appendix A: Excitation energy flux

Population non-equilibrium fluxes can be easily determined from the solution to a Pauli (population only) master equation, as done for example in Ref. 39. It is more complicated to determine these fluxes from a quantum master equation, because in the site basis coherences are also involved. We can start from the formal solution to a Markovian quantum master equation,

$$\rho_{ab}^S(t + \Delta t) = \sum_{cd} \mathcal{U}_{ab,cd}(\Delta t) \rho_{cd}^S(t) \quad (\text{A1})$$

where $\mathcal{U}(\Delta t) = e^{\frac{i}{\hbar} \mathcal{L} \Delta t}$ propagates the density matrix from time 0 to time t and $\mathcal{L}_{ab,cd} = R_{ab,cd} + i \omega_{cd} \delta_{ac} \delta_{bd}$ is the representation tensor of the Liouvillian superoperator in exciton basis.

The density matrix evolution can be written in the site basis,

$$\rho_{ij}^S(t + \Delta t) = \sum_{kl} U_{kl \rightarrow ij}(\Delta t) \rho_{kl}^S(t) \quad (\text{A2})$$

where

$$U_{kl \rightarrow ij}(\Delta t) = \sum_{abcd} c_{ia} c_{jb} c_{kc} c_{ld} U_{cd \rightarrow ab}(\Delta t) \quad (\text{A3})$$

We can define the net flux from any population or coherence ρ_{kl}^S to another ρ_{ij}^S from time t to time $t + \Delta t$ as the following expression:

$$\Phi_{kl \rightarrow ij}(t \rightarrow t + \Delta t) = U_{kl \rightarrow ij}(\Delta t) \rho_{kl}^S(t) - U_{ij \rightarrow kl}(\Delta t) \rho_{ij}^S(t) \quad (\text{A4})$$

Finally, we take the population-only elements of Φ to define the population flux between sites

$$\tilde{\Phi}_{k \rightarrow j}(t \rightarrow t + \Delta t) = U_{kk \rightarrow jj}(\Delta t) \rho_{kk}^S(t) - U_{jj \rightarrow kk}(\Delta t) \rho_{jj}^S(t) \quad (\text{A5})$$

Equation A5 can be interpreted as follows: the terms $U_{kk \rightarrow jj}(\Delta t)$ dictate how the matrix element ρ_{kk}^S evolves after a time Δt , i.e. the fraction of the population on site k that is transferred to each site j . This term is multiplied by the population at the beginning of the investigated time window, $\rho_{kk}^S(t)$, so that the product quantifies the amount of population transferred between the sites k and j . Finally, the terms $k \rightarrow j$ and $j \rightarrow k$ are subtracted in order to consider only the net flux in one direction. Finally, the quantity $\tilde{\Phi}_{k \rightarrow j}$ can be calculated for each realization of the static disorder, and then averaged over the entire ensemble.

Appendix B: Effective rates

Given the total Liouvillian \mathcal{L} , one can retrieve a rate matrix in the site basis assuming that after a certain time Δt the site-population dynamics becomes effectively Markovian. This may occur when the fastest processes have finished and a steady state of lower dimensionality is approached.

To this purpose, the operator on the population subspace in the site basis is compared to that of a rate equation

$$U_{jj \rightarrow ii}^{pop}(\Delta t) = e^{K \Delta t}$$

which means that the rate matrix K can be computed as the matrix logarithm of $U^{pop}(\Delta t)$, divided by Δt .

We sum the rates belonging to the same exciton domain using the Boltzmann population as weight for the summation, assuming that thermal equilibrium has established between the chromophores belonging to the same clusters⁷⁴. If we indicate the thermal population with $P(\infty)$ and $Z_B = \sum_{j \in B} P_j(\infty)$, the partitioned rate matrix \tilde{K} can be computed as before, using the following relation:

$$\left(e^{K \Delta t} \right)_{B \rightarrow A} = \sum_{i \in A} \sum_{j \in B} \frac{P_j(\infty)}{Z} \left(e^{K \Delta t} \right)_{j \rightarrow i} \quad (\text{B1})$$

Summing up, to determine average rates in the disordered exciton system, we first compute the propagator $U^{pop}(\Delta t)$ for each realizations of the disorder, then we determine the rate matrix K . After this, we lump the rate matrices of each realization using eq. (B1) and, finally, we average K over the static disorder.

It is entirely possible that K contains negative off-diagonal elements, i.e. “unphysical” rates (See Table S2), which means that it is not possible to describe the (Markovian) evolution of the population as a Pauli master equation. This problem can arise from the loss of information on the state of the system when the latter is described only with populations of pigments or domains. Notwithstanding these limitations, we can still take the positive elements of the rate matrix as a faithful representation of the effective rates in the exciton system.

REFERENCES

- 1T. Mirkovic, E. E. Ostroumov, J. M. Anna, R. van Grondelle, Govindjee, and G. D. Scholes, “Light absorption and energy transfer in the antenna complexes of photosynthetic organisms,” *Chemical Reviews* **117**, 249–293 (2017).
- 2G. D. Scholes, G. R. Fleming, A. Olaya-Castro, and R. van Grondelle, “Lessons from nature about solar light harvesting,” *Nat. Chem.* **3**, 763–774 (2011).
- 3R. Croce and H. van Amerongen, “Natural strategies for photosynthetic light harvesting,” *Nature Chemical Biology* **10**, 492–501 (2014).
- 4M. Ballottari, J. Girardon, L. Dall’Osto, and R. Bassi, “Evolution and functional properties of Photosystem II light harvesting complexes in eukaryotes,” *Biochim. Biophys. Acta (BBA) - Bioenerg.* **1817**, 143–157 (2012).
- 5R. Berera, R. van Grondelle, and J. T. M. Kennis, “Ultrafast transient absorption spectroscopy: principles and application to photosynthetic systems,” *Photosynth. Res.* **101**, 105–118 (2009).
- 6P. H. Lambrev, P. Akhtar, and H. S. Tan, “Insights into the mechanisms and dynamics of energy transfer in plant light-harvesting complexes from two-dimensional electronic spectroscopy,” *Biochim. Biophys. Acta - Bioenerg.* **1861**, 148050 (2020).

- ⁷O. C. Fiebig, D. Harris, D. Wang, M. P. Hoffmann, and G. S. Schlau-Cohen, "Ultrafast dynamics of photosynthetic light harvesting: Strategies for acclimation across organisms," *Annu. Rev. Phys. Chem.* **74**, 493–520 (2023).
- ⁸Y.-C. Cheng and G. R. Fleming, "Dynamics of light harvesting in photosynthesis," *Annual Review of Physical Chemistry* **60**, 241–262 (2009).
- ⁹V. I. Novoderezhkin, M. A. Palacios, H. van Amerongen, and R. van Grondelle, "Energy-transfer dynamics in the LHCII complex of higher plants: Modified redfield approach," *J. Phys. Chem. B* **108**, 10363–10375 (2004).
- ¹⁰V. I. Novoderezhkin, M. A. Palacios, H. van Amerongen, and R. van Grondelle, "Excitation Dynamics in the LHCII Complex of Higher Plants: Modeling Based on the 2.72 Å Crystal Structure," *J. Phys. Chem. B* **109**, 10493–10504 (2005).
- ¹¹V. I. Novoderezhkin, A. B. Doust, C. Curutchet, G. D. Scholes, and R. van Grondelle, "Excitation dynamics in phycoerythrin 545: Modeling of steady-state spectra and transient absorption with modified redfield theory," *Biophys. J.* **99**, 344–352 (2010).
- ¹²V. Novoderezhkin, A. Marin, and R. V. Grondelle, "Intra- and intermonomeric transfers in the light harvesting LHCII complex: The Redfield-Förster picture," *Physical Chemistry Chemical Physics* **13**, 17093–17103 (2011).
- ¹³N. Liguori, V. Novoderezhkin, L. M. Roy, R. Van Grondelle, and R. Croce, "Excitation dynamics and structural implication of the stress-related complex LHCSR3 from the green alga *Chlamydomonas reinhardtii*," *Biochim. Biophys. Acta - Bioenerg.* **1857**, 1514–1523 (2016).
- ¹⁴V. I. Novoderezhkin and R. Croce, "The location of the low-energy states in lhca1 favors excitation energy transfer to the core in the plant PSI-LHCI supercomplex," *Photosynth. Res.* **156**, 59–74 (2023).
- ¹⁵M. Jassas, J. Chen, A. Khmel'nitskiy, A. P. Casazza, S. Santabarbara, and R. Jankowiak, "Structure-based exciton hamiltonian and dynamics for the reconstituted wild-type CP29 protein antenna complex of the photosystem II," *Journal of Physical Chemistry B* **122**, 4611–4624 (2018).
- ¹⁶F. Müh, M. E.-A. Madjet, and T. Renger, "Structure-Based Identification of Energy Sinks in Plant Light-Harvesting Complex II," *J. Phys. Chem. B* **114**, 13517–13535 (2010).
- ¹⁷V. I. Novoderezhkin and R. van Grondelle, "Physical origins and models of energy transfer in photosynthetic light-harvesting," *Phys. Chem. Chem. Phys.* **12**, 7352 (2010).
- ¹⁸T. Renger and F. Müh, "Understanding photosynthetic light-harvesting: a bottom up theoretical approach," *Phys. Chem. Chem. Phys.* **15**, 3348 (2013).
- ¹⁹C. Olbrich, T. L. C. Jansen, J. Liebers, M. Aghtar, J. Strümpfer, K. Schulten, J. Knoester, and U. Kleinekathöfer, "From Atomistic Modeling to Excitation Transfer and Two-Dimensional Spectra of the FMO Light-Harvesting Complex," *J. Phys. Chem. B* **115**, 8609–8621 (2011).
- ²⁰T. Renger, M. E.-A. Madjet, M. S. am Busch, J. Adolphs, and F. Müh, "Structure-based modeling of energy transfer in photosynthesis," *Photosynthesis Research* **116**, 367–388 (2013).
- ²¹S. Maity and U. Kleinekathöfer, "Recent progress in atomistic modeling of light-harvesting complexes: a mini review," *Photosynth. Res.* **156**, 147–162 (2023).
- ²²C. Curutchet and B. Mennucci, "Quantum chemical studies of light harvesting," *Chem. Rev.* **117**, 294–343 (2017).
- ²³F. Segatta, L. Cupellini, M. Garavelli, and B. Mennucci, "Quantum Chemical Modeling of the Photoinduced Activity of Multichromophoric Biosystems," *Chem. Rev.* **119**, 9361–9380 (2019).
- ²⁴L. Cupellini, M. Bondanza, M. Nottoli, and B. Mennucci, "Successes & challenges in the atomistic modeling of light-harvesting and its photoregulation," *Biochim. Biophys. Acta (BBA) - Bioenerg.* **1861**, 148049 (2020).
- ²⁵E. Cignoni, V. Slama, L. Cupellini, and B. Mennucci, "The atomistic modeling of light-harvesting complexes from the physical models to the computational protocol," *J. Chem. Phys.* **156**, 120901 (2022).
- ²⁶V. Sláma, L. Cupellini, and B. Mennucci, "Exciton properties and optical spectra of light harvesting complex II from a fully atomistic description," *Phys. Chem. Chem. Phys.* **22**, 16783–16795 (2020).
- ²⁷F. C. Ramos, M. Nottoli, L. Cupellini, and B. Mennucci, "The molecular mechanisms of light adaption in light-harvesting complexes of purple bacteria revealed by a multiscale modeling," *Chem. Sci.* **10**, 9650–9662 (2019).
- ²⁸I. Guarnetti Prandi, V. Sláma, C. Pecorilla, L. Cupellini, and B. Mennucci, "Structure of the stress-related LHCSR1 complex determined by an integrated computational strategy," *Commun. Biol.* **5**, 145 (2022).
- ²⁹L. Cupellini, P. Qian, T. C. Nguyen-Phan, A. T. Gardiner, and R. J. Cogdell, "Quantum chemical elucidation of a sevenfold symmetric bacterial antenna complex," *Photosynth. Res.* **156**, 75–87 (2022).
- ³⁰M. Bondanza, M. Nottoli, L. Cupellini, F. Lipparini, and B. Mennucci, "Polarizable embedding QM/MM: the future gold standard for complex (bio)systems?" *Phys. Chem. Chem. Phys.* **22**, 14433–14448 (2020).
- ³¹F. Segatta, L. Cupellini, S. Jurinovich, S. Mukamel, M. Dapor, S. Taioli, M. Garavelli, and B. Mennucci, "A quantum chemical interpretation of two-dimensional electronic spectroscopy of light-harvesting complexes," *Journal of the American Chemical Society* **139**, 7558–7567 (2017).
- ³²X. Pan, M. Li, T. Wan, L. Wang, C. Jia, Z. Hou, X. Zhao, J. Zhang, and W. Chang, "Structural insights into energy regulation of light-harvesting complex CP29 from spinach," *Nat. Struct. Mol. Biol.* **18**, 309–15 (2011).
- ³³X. Pan, Z. Liu, M. Li, and W. Chang, "Architecture and function of plant light-harvesting complexes II," *Curr. Opin. Struct. Biol.* **23**, 515–25 (2013).
- ³⁴X. Wei, X. Su, P. Cao, X. Liu, W. Chang, M. Li, X. Zhang, and Z. Liu, "Structure of spinach photosystem II-LHCII supercomplex at 3.2 Å resolution," *Nature* **534**, 69–74 (2016).
- ³⁵X. Su, J. Ma, X. Wei, P. Cao, D. Zhu, W. Chang, Z. Liu, X. Zhang, and M. Li, "Structure and assembly mechanism of plant c2s2m2-type psii-lhcii supercomplex," *Science* **357**, 815–820 (2017).
- ³⁶F. Müh, D. Lindorfer, M. S. A. Busch, and T. Renger, "Towards a structure-based exciton hamiltonian for the CP29 antenna of photosystem II," *Physical Chemistry Chemical Physics* **16**, 11848–11863 (2014).
- ³⁷K. F. Fox, C. Ünlü, V. Balevičius, B. N. Ramdour, C. Kern, X. Pan, M. Li, H. van Amerongen, and C. D. Duffy, "A possible molecular basis for photoprotection in the minor antenna proteins of plants," *Biochimica et Biophysica Acta - Bioenergetics* **1859**, 471–481 (2018).
- ³⁸V. Mascoli, V. Novoderezhkin, N. Liguori, P. Xu, and R. Croce, "Design principles of solar light harvesting in plants: Functional architecture of the monomeric antenna CP29," *Biochim. Biophys. Acta (BBA) - Bioenerg.* **1861**, 148156 (2020).
- ³⁹M. Lapillo, E. Cignoni, L. Cupellini, and B. Mennucci, "The energy transfer model of nonphotochemical quenching: Lessons from the minor CP29 antenna complex of plants," *Biochim. Biophys. Acta (BBA) - Bioenerg.* **1861**, 148282 (2020).
- ⁴⁰S. Sardar, R. Caferri, F. V. A. Camargo, J. P. Serrano, A. Ghezzi, S. Capaldi, L. Dall'Osto, R. Bassi, C. D'Andrea, and G. Cerullo, "Molecular mechanisms of light harvesting in the minor antenna CP29 in near-native membrane lipidic environment," *J. Chem. Phys.* **156**, 205101 (2022).
- ⁴¹G. Raszewski, W. Saenger, and T. Renger, "Theory of optical spectra of photosystem II reaction centers: Location of the triplet state and the identity of the primary electron donor," *Biophys. J.* **88**, 986–998 (2005).
- ⁴²J. Ma and J. Cao, "Förster resonance energy transfer, absorption and emission spectra in multichromophoric systems. i. full cumulant expansions and system-bath entanglement," *J. Chem. Phys.* **142**, 094106 (2015).
- ⁴³L. Cupellini, F. Lipparini, and J. Cao, "Absorption and circular dichroism spectra of molecular aggregates with the full cumulant expansion," *J. Phys. Chem. B* **124**, 8610–8617 (2020).
- ⁴⁴J. A. Nöthling, T. Mančal, and T. P. J. Krüger, "Accuracy of approximate methods for the calculation of absorption-type linear spectra with a complex system-bath coupling," *J. Chem. Phys.* **157**, 095103 (2022).
- ⁴⁵A. Gelzinis, D. Abramavicius, and L. Valkunas, "Absorption lineshapes of molecular aggregates revisited," *J. Chem. Phys.* **142**, 154107 (2015).
- ⁴⁶T. Renger and R. A. Marcus, "On the relation of protein dynamics and exciton relaxation in pigment-protein complexes: An estimation of the spectral density and a theory for the calculation of optical spectra," *J. Chem. Phys.* **116**, 9997–10019 (2002).
- ⁴⁷D. Abramavicius, B. Palmieri, D. V. Voronine, F. Šanda, and S. Mukamel, "Coherent Multidimensional Optical Spectroscopy of Excitons in Molecular Aggregates: Quasiparticle versus Supermolecule Perspectives," *Chem. Rev.* **109**, 2350–2408 (2009).
- ⁴⁸L. Röss, P. Malý, J. B. Landgraf, D. Lindorfer, M. Hofer, J. Selby, C. Lambert, T. Renger, and T. Brixner, "Time-resolved circular dichroism of excitonic systems: Theory and experiment on an exemplary squaraine polymer," *Chem. Sci.*, DOI: 10.1039/d3sc01674a (2023).
- ⁴⁹J. Adolphs and T. Renger, "How Proteins Trigger Excitation Energy Transfer in the FMO Complex of Green Sulfur Bacteria," *Biophys. J.* **91** (2006), 10.1529/biophysj.105.079483.

- ⁵⁰O. Rancova, R. Jankowiak, and D. Abramavicius, "Role of bath fluctuations in the double-excitation manifold in shaping the 2DES of bacterial reaction centers at low temperature," *J. Phys. Chem. B* **122**, 1348–1366 (2018).
- ⁵¹M. Yang, A. Damjanović, H. M. Vaswani, and G. R. Fleming, "Energy transfer in photosystem i of cyanobacteria *synechococcus elongatus*: Model study with structure-based semi-empirical hamiltonian and experimental spectral density," *Biophys. J.* **85**, 140–158 (2003).
- ⁵²H. Sumi, "Theory on Rates of Excitation-Energy Transfer between Molecular Aggregates through Distributed Transition Dipoles with Application to the Antenna System in Bacterial Photosynthesis," *J. Phys. Chem. B* **103**, 252–260 (1999).
- ⁵³G. D. Scholes, X. J. Jordanides, and G. R. Fleming, "Adapting the Förster theory of energy transfer for modeling dynamics in aggregated molecular assemblies," *J. Phys. Chem. B* **105**, 1640–1651 (2001).
- ⁵⁴S. Jang, M. D. Newton, and R. J. Silbey, "Multichromophoric Förster resonance energy transfer," *Phys. Rev. Lett.* **92**, 218301 (2004).
- ⁵⁵Z. Guardini, M. Bressan, R. Caferri, R. Bassi, and L. Dall'Osto, "Identification of a pigment cluster catalysing fastphotoprotective quenching response in CP29," *Nat. Plants* **6**, 303–313 (2020).
- ⁵⁶C. Curutchet, A. Muñoz Losa, S. Monti, J. Kongsted, G. D. Scholes, and B. Mennucci, "Electronic Energy Transfer in Condensed Phase Studied by a Polarizable QM/MM Model," *J. Chem. Theory Comput.* **5**, 1838–1848 (2009).
- ⁵⁷M. J. Frisch, G. W. Trucks, H. B. Schlegel, G. E. Scuseria, M. A. Robb, J. R. Cheeseman, G. Scalmani, V. Barone, G. A. Petersson, H. Nakatsuji, X. Li, M. Caricato, A. V. Marenich, J. Bloino, B. G. Janesko, R. Gomperts, B. Mennucci, H. P. Hratchian, J. V. Ortiz, A. F. Izmaylov, J. L. Sonnenberg, D. Williams-Young, F. Ding, F. Lipparini, F. Egidi, J. Goings, B. Peng, A. Petrone, T. Henderson, D. Ranasinghe, V. G. Zakrzewski, J. Gao, N. Rega, G. Zheng, W. Liang, M. Hada, M. Ehara, K. Toyota, R. Fukuda, J. Hasegawa, M. Ishida, T. Nakajima, Y. Honda, O. Kitao, H. Nakai, T. Vreven, K. Throssell, J. A. Montgomery, Jr., J. E. Peralta, F. Ogliaro, M. J. Bearpark, J. J. Heyd, E. N. Brothers, K. N. Kudin, V. N. Staroverov, T. A. Keith, R. Kobayashi, J. Normand, K. Raghavachari, A. P. Rendell, J. C. Burant, S. S. Iyengar, J. Tomasi, M. Cossi, J. M. Millam, M. Klene, C. Adamo, R. Cammi, J. W. Ochterski, R. L. Martin, K. Morokuma, O. Farkas, J. B. Foresman, and D. J. Fox, "Gaussian-16 Revision C.01," (2016), gaussian Inc. Wallingford CT.
- ⁵⁸J. Wang, P. Cieplak, J. Li, T. Hou, R. Luo, and Y. Duan, "Development of polarizable models for molecular mechanical calculations i: Parameterization of atomic polarizability," *J. Phys. Chem. B* **115**, 3091–3099 (2011).
- ⁵⁹S. Mukamel, *Principles of Nonlinear Optical Spectroscopy*, Oxford series in optical and imaging sciences (Oxford University Press, 1995).
- ⁶⁰M. K. Lee, P. Huo, and D. F. Coker, "Semiclassical path integral dynamics: Photosynthetic energy transfer with realistic environment interactions," *Annu. Rev. Phys. Chem.* **67**, 639–668 (2016).
- ⁶¹S. Maity, P. Sarngadharan, V. Daskalakis, and U. Kleinekathöfer, "Time-dependent atomistic simulations of the CP29 light-harvesting complex," *Journal of Chemical Physics* **155** (2021), 10.1063/5.0053259.
- ⁶²S. Jurinovich, L. Viani, I. G. Prandi, T. Renger, and B. Mennucci, "Towards an ab initio description of the optical spectra of light-harvesting antennae: application to the CP29 complex of photosystem II," *Phys. Chem. Chem. Phys.* **17**, 14405–16 (2015).
- ⁶³S. Petry, J. C. Tremblay, and J. P. Götze, "Impact of structural sampling, coupling scheme and state of interest on the energy transfer in CP29," *bioRxiv* (2023), 10.1101/2023.01.25.525376, <https://www.biorxiv.org/content/10.1101/2023.01.25.525376v1>.
- ⁶⁴A. Gelzinis and L. Valkunas, "Analytical derivation of equilibrium state for open quantum system," *Journal of Chemical Physics* **152** (2020), 10.1063/1.5141519.
- ⁶⁵T.-C. Dinh and T. Renger, "Towards an exact theory of linear absorbance and circular dichroism of pigment-protein complexes: Importance of non-secular contributions," *J. Chem. Phys.* **142**, 034104 (2015).
- ⁶⁶A. G. Dijkstra, T. la Cour Jansen, and J. Knoester, "Localization and coherent dynamics of excitons in the two-dimensional optical spectrum of molecular J-aggregates," *J. Chem. Phys.* **128**, 164511 (2008).
- ⁶⁷A. Gelzinis, D. Abramavicius, and L. Valkunas, "Non-Markovian effects in time-resolved fluorescence spectrum of molecular aggregates: Tracing polaron formation," *Phys. Rev. B* **84** (2011), 10.1103/PhysRevB.84.245430.
- ⁶⁸J. M. Moix, Y. Zhao, and J. Cao, "Equilibrium-reduced density matrix formulation: Influence of noise, disorder, and temperature on localization in excitonic systems," *Phys. Rev. B* **85**, 115412 (2012).
- ⁶⁹Y. Yan, Y. Liu, T. Xing, and Q. Shi, "Theoretical study of excitation energy transfer and nonlinear spectroscopy of photosynthetic light-harvesting complexes using the nonperturbative reduced dynamics method," *WIREs Comput. Mol. Sci.* **11** (2020), 10.1002/wcms.1498.
- ⁷⁰Y. Tanimura, "Numerically "exact" approach to open quantum dynamics: The hierarchical equations of motion (HEOM)," *J. Chem. Phys.* **153** (2020), 10.1063/5.0011599.
- ⁷¹S. Kundu and N. Makri, "Intramolecular vibrations in excitation energy transfer: Insights from real-time path integral calculations," *Annu. Rev. Phys. Chem.* **73**, 349–375 (2022).
- ⁷²T. P. Fay and D. T. Limmer, "Coupled charge and energy transfer dynamics in light harvesting complexes from a hybrid hierarchical equations of motion approach," *J. Chem. Phys.* **157**, 174104 (2022).
- ⁷³J. H. Fetherolf and T. C. Berkelbach, "Linear and Nonlinear Spectroscopy from Quantum Master Equations," *J. Chem. Phys.* **147**, 244109 (2017).
- ⁷⁴Y. Shibata, S. Nishi, K. Kawakami, J.-R. Shen, and T. Renger, "Photosystem II does not possess a simple excitation energy funnel: Time-resolved fluorescence spectroscopy meets theory," *Journal of the American Chemical Society* **135**, 6903–6914 (2013).